Nanometre-scale thermometry in a living cell

LETTER

doi:10.1038/nature12373

Nanometre-scale thermometry in a living cell

G. Kucsko[1]*, P. C. Maurer[1]*, N. Y. Yao[1], M. Kubo[2], H. J. Noh[3], P. K. Lo[4], H. Park[1,2,3] & M. D. Lukin[1]

Sensitive probing of temperature variations on nanometre scales is an outstanding challenge in many areas of modern science and technology[1]. In particular, a thermometer capable of subdegree temperature resolution over a large range of temperatures as well as integration within a living system could provide a powerful new tool in many areas of biological, physical and chemical research. Possibilities range from the temperature-induced control of gene expression[2–5] and tumour metabolism[6] to the cell-selective treatment of disease[7,8] and the study of heat dissipation in integrated circuits[1]. By combining local light-induced heat sources with sensitive nanoscale thermometry, it may also be possible to engineer biological processes at the subcellular level[2–5]. Here we demonstrate a new approach to nanoscale thermometry that uses coherent manipulation of the electronic spin associated with nitrogen–vacancy colour centres in diamond. Our technique makes it possible to detect temperature variations as small as 1.8 mK (a sensitivity of 9 mK $Hz^{-1/2}$) in an ultrapure bulk diamond sample. Using nitrogen–vacancy centres in diamond nanocrystals (nanodiamonds), we directly measure the local thermal environment on length scales as short as 200 nanometres. Finally, by introducing both nanodiamonds and gold nanoparticles into a single human embryonic fibroblast, we demonstrate temperature-gradient control and mapping at the subcellular level, enabling unique potential applications in life sciences.

Many promising approaches to local temperature sensing[1] are being explored at present. These include scanning probe microscopy[1,9], Raman spectroscopy[10], and fluorescence-based measurements using nanoparticles[11,12] and organic dyes[13,14]. Fluorescent polymers[13] and green fluorescent proteins[14] have recently been used for temperature mapping within a living cell. However, many of these existing methods are limited by drawbacks such as low sensitivity and systematic errors due to fluctuations in the fluorescence rate[11,12], the local chemical environment[13] and the optical properties of the surrounding medium[14]. Moreover, although promising, methods based on green fluorescent proteins rely on cellular transfection[14] that proves to be difficult to achieve in certain primary cell types[15]. Our new approach to nanoscale thermometry uses the quantum mechanical spin associated with nitrogen–vacancy colour centres in diamond. As illustrated in Fig. 1b, in its electronic ground state each nitrogen–vacancy centre constitutes a spin-1 system. These spin states can be coherently manipulated using microwave pulses and efficiently initialized and detected by means of laser illumination (Supplementary Information). In the absence of an external magnetic field, the precise value of the transition frequency

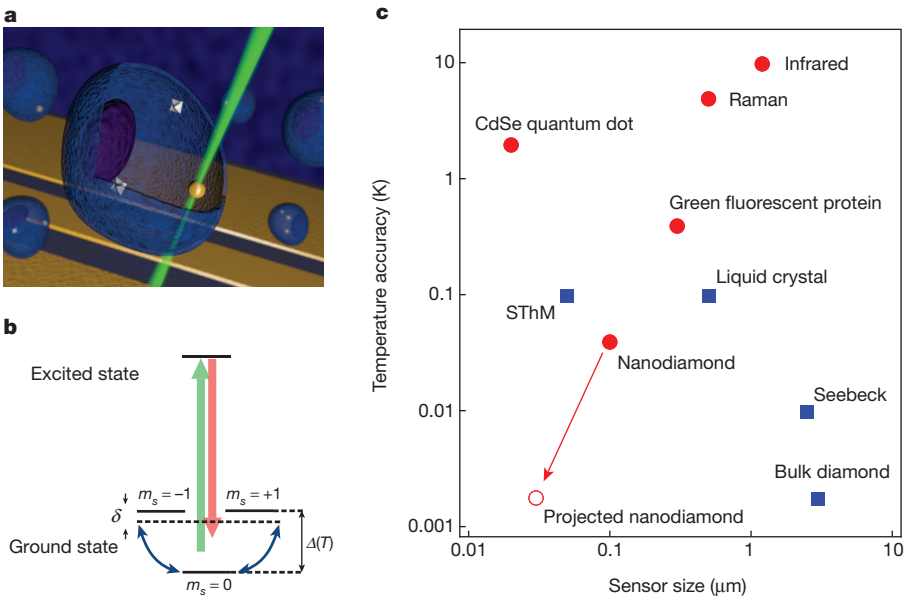

Figure 1 | Nitrogen–vacancy-based nanoscale thermometry. a, Schematic image depicting nanodiamonds (grey diamonds) and a gold nanoparticle (yellow sphere) within a living cell (central blue object; others are similar) with coplanar waveguide (yellow stripes) in the background. The controlled application of local heat is achieved by laser illumination of the gold nanoparticle, and nanoscale thermometry is achieved by precision spectroscopy of the nitrogen–vacancy spins in the nanodiamonds. **b**, Simplified nitrogen–vacancy level diagram showing a ground-state spin triplet and an excited state. At zero magnetic field, the $|\pm1\rangle$ sublevels are split from the $|0\rangle$ state by a temperature-dependent zero field splitting $\Delta(T)$. Pulsed microwave radiation is applied (detuning, δ) to perform Ramsey-type spectroscopy. **c**, Comparison of sensor sizes and temperature accuracies for the nitrogen–vacancy quantum thermometer and other reported techniques. Red circles indicate methods that are biologically compatible. The open red circle indicates the ultimate expected accuracy for our measurement technique in solution (Methods).

[1]Department of Physics, Harvard University, Cambridge, Massachusetts 02138, USA. [2]Department of Chemistry and Chemical Biology, Harvard University, Cambridge, Massachusetts 02138, USA. [3]Broad Institute of MIT and Harvard University, 7 Cambridge Center, Cambridge, Massachusetts 02142, USA. [4]Department of Biology and Chemistry, City University of Hong Kong, Tat Chee Avenue, Kowloon, Hong Kong SAR, China.
*These authors contributed equally to this work.

(Δ) between the $|m_s = 0\rangle$ and $|m_s = \pm 1\rangle$ states (m_s, spin projection) has a temperature dependence ($\mathrm{d}\Delta/\mathrm{d}T = -2\pi \times 77\,\mathrm{kHz\,K^{-1}}$) due to thermally induced lattice strains[16–18].

The operational principle of nitrogen–vacancy-based thermometry relies on the accurate measurement of this transition frequency, which can be optically detected with high spatial resolution (Fig. 1). For a sensor containing N colour centres, the temperature sensitivity is given by

$$\eta = \frac{1}{C\mathrm{d}\Delta/\mathrm{d}T}\frac{1}{\sqrt{T_{\mathrm{coh}}Nt}}$$

where T_{coh} is the nitrogen–vacancy spin coherence time and t is the integration time. Here we also introduce a factor, C, to account for imperfections in readout and initialization[19]. If T_{coh} is of the order of a few milliseconds and $C \approx 0.03$ (ref. 19), then a single nitrogen–vacancy can potentially exhibit a sensitivity better than $1\,\mathrm{mK\,Hz^{-1/2}}$. Apart from high sensitivity, nitrogen–vacancy-based thermometry also offers several distinct advantages over existing methods in biological and chemical temperature sensing. First, owing to diamond's chemical inertness, it is generally robust to changes in the local chemical environment. Second, it can be applied over a wide range of temperatures (200–600 K; refs 17, 18), which is of particular interest in the study of nanoscale chemical reactions[20].

As a benchmark experiment, we demonstrate the high temperature sensitivity of nitrogen–vacancy-based thermometry in a bulk diamond sample. Although the nitrogen–vacancy's magnetic sensitivity has rendered it a competitive magnetometer[21,22], to determine the temperature accurately it is necessary to decouple the nitrogen–vacancy electronic spin from fluctuating external magnetic fields. This is achieved using a modified spin-echo sequence that makes use of the spin-1 nature of the nitrogen–vacancy defect[23], allowing us to eliminate the effects of an external, slowly varying magnetic field. Specifically, we apply a microwave pulse at frequency ω (Fig. 1b) to create a coherent superposition $(|0\rangle + |B\rangle)/\sqrt{2}$, where $|B\rangle = (|+1\rangle + |-1\rangle)/\sqrt{2}$. After half the total evolution time, τ, we apply a 2π echo pulse that swaps the population of the $|+1\rangle$ and $|-1\rangle$ states (Fig. 2a). Following another period of free evolution for time τ, quasistatic, magnetic-field-induced shifts of these $|\pm 1\rangle$ levels are eliminated, allowing for accurate temperature sensing. In the experiment, we use a sample of isotopically pure diamond (99.99% spinless ^{12}C isotope) grown by chemical vapour deposition[24] to further reduce magnetic field fluctuations originating from the intrinsic ^{13}C nuclear spin bath. As shown in Fig. 2a, this allows us to observe coherence fringes for up to 0.5 ms. Notably, for all nitrogen–vacancies tested, we observe a characteristic low-frequency beating of the fluorescence signal that varies from defect to defect, which is most probably due to locally fluctuating charge traps[25]. Despite this beating, for a fixed evolution time 2τ, the nitrogen–vacancy spin depends sensitively on the sample temperature (Fig. 2b). We observe a temperature sensitivity of $\eta = (9 \pm 1.8)\,\mathrm{mK\,Hz^{-1/2}}$ for $2\tau = 250\,\mu\mathrm{s}$. For 30 s of integration, we achieve a measurement accuracy of $\delta T = 1.8 \pm 0.3\,\mathrm{mK}$ (Methods). Although the measurement sequence for a single value of 2τ allows us to determine the temperature only up to a multiple of $(2\mathrm{d}\Delta/\mathrm{d}T2\tau)^{-1}$, absolute temperature variations can be determined by repeating the measurement for $2\tau' < 2\tau$, as shown in Fig. 2b.

We now demonstrate the high spatial resolution of nitrogen–vacancy-based thermometry. This is achieved by using nanodiamonds. In most commercially available nanodiamonds, the nitrogen–vacancy coherence time is limited to approximately 1 μs owing to additional paramagnetic impurities. Although this shortened coherence time reduces the intrinsic temperature sensitivity for a single defect, this decrease can be offset by using an ensemble of nitrogen–vacancies to enhance the signal-to-noise ratio by a factor of $\sqrt{N}$. We note that, unlike nitrogen–vacancy-based magnetometry, where the proximity to the source (often limited by the nanodiamond size) is critical to the maximum sensitivity, nitrogen–vacancy thermometry is not subject to such a constraint; in fact, the excellent thermal conductivity of diamond ensures that all nitrogen–vacancy centres within a nanocrystal are in thermal equilibrium with the local heat environment. To maximize the number of nitrogen–vacancy centres and to minimize the lattice strain, our measurements are performed on single-crystalline nanodiamonds containing approximately 500 nitrogen–vacancy centres (Adamas Nanotechnologies). The zero-field splitting, Δ, of the nitrogen–vacancy ensemble, and, thus, the temperature, is determined by recording a continuous-wave electron spin resonance (ESR) spectrum. Specifically, we measure changes to the zero-field splitting by recording the fluorescence at four different frequencies centred around $\Delta = 2\pi \times 2.87\,\mathrm{GHz}$ (Fig. 3a). This procedure eliminates unwanted effects from fluctuations in the total fluorescence rate, ESR contrast, Rabi frequency and magnetic field, yielding a robust thermometer (Methods).

Combining our nanodiamond thermometer with the laser heating of a gold nanoparticle allows us to both monitor and control temperature at nanometre length scales (Fig. 3). Both nanodiamonds and gold nanoparticles (nominal diameter, 100 nm) are initially spin-coated on a microscope coverslip. Using a confocal microscope with two independent scanning beams, we co-localize gold nanoparticles and nanodiamonds

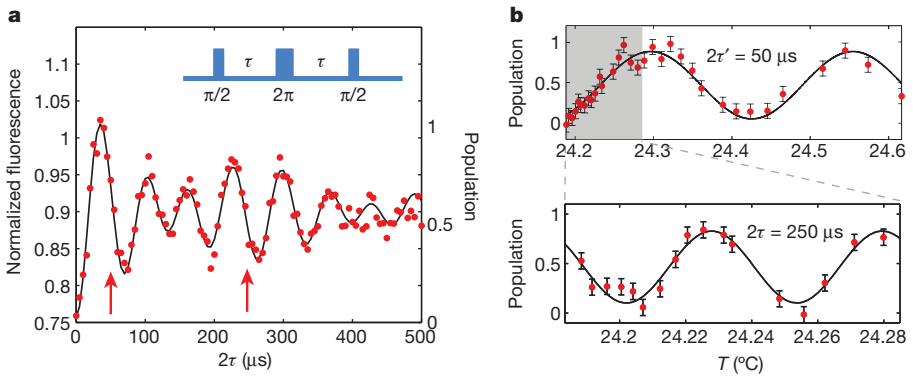

Figure 2 | Sensitivity of single nitrogen–vacancy thermometer. a, Measured fluorescence as a function of echo evolution time, 2τ (red points); the black solid line indicates a fit corresponding to a damped cosine function with two distinct frequencies. The characteristic beating can be explained by fluctuating proximal charge traps separated from the nitrogen–vacancy centre by a distance of about 50 nm. Inset, the microwave 2π echo pulse sequence used to cancel unwanted external magnetic field fluctuations[23]. **b**, Measured fluorescence (red points) as a function of temperature for echo times of $2\tau = 250\,\mu\mathrm{s}$ (bottom) and $2\tau' = 50\,\mu\mathrm{s}$ (top). Black lines, best fits; errors, 1σ. The fixed evolution times of 2τ and $2\tau'$ are indicated in **a** by red arrows. The temperature is controlled by a Peltier element at the sample mount, and the (local) x-axis temperature is determined using a thermistor located immediately next to the sample. The fluorescence is converted to population by normalizing to two reference measurements where the spin is prepared with $m_s = 0$ and, respectively, $m_s = -1$.

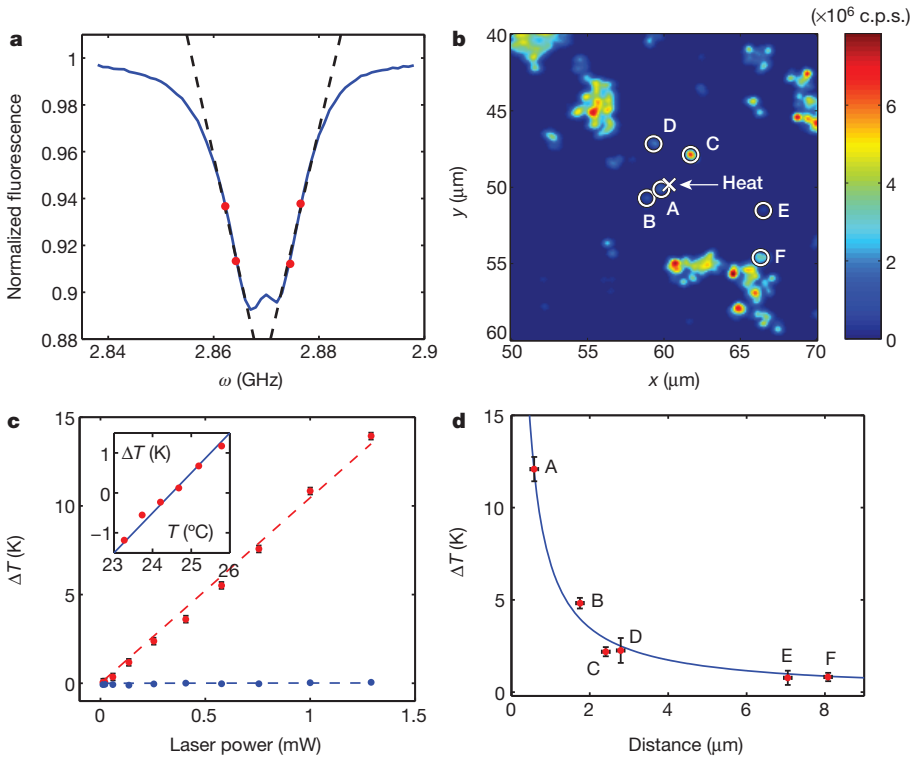

Figure 3 | Submicrometre thermometry using nanodiamonds. **a**, Frequency scan of a single nanodiamond containing approximately 500 nitrogen–vacancy centres. The four red points indicate the measurement frequencies used to extract the temperature as detailed in Methods. **b**, Two-dimensional confocal scan of nanodiamonds (circles) and a gold nanoparticle (cross) spin-coated onto a glass coverslip. The colour bar represents fluorescence, expressed in counts per second (c.p.s.). **c**, Temperature of a single nanodiamond as a function of laser power for two different laser focus locations. The red data points depict the pronounced heating of a nanodiamond as a result of laser illumination of a nearby gold nanoparticle. The blue data points depict the same measurement with the laser focus displaced by 0.8 μm from the nanoparticle location; this results in negligible heating of the nanodiamond as a function of laser power. Inset, the measured temperature change of a nanodiamond, when the surrounding temperature is controlled by a Peltier element. **d**, Temperature changes measured (red points) at the six nanodiamond locations in **b** as a function of distance from the illuminated gold nanoparticle (cross). The blue curve is the theoretical temperature profile based on a steady-state solution of the heat equation. All data in this figure were obtained on a glass coverslip, and all error bars correspond to 1σ.

with a resolution of ~100 nm (Supplementary Information). While locally heating the gold nanoparticles by continuous illumination with a variable-power green laser (focused to a diffraction-limited spot), we simultaneously measure the temperature at the nanodiamond location using ESR spectroscopy.

The ability to measure temperature with nanodiamonds is verified by heating the substrate temperature over a range of 2.5 K and simultaneously monitoring the zero-field splitting (Fig. 3c, inset). To demonstrate nanoscale temperature control, in Fig. 3c (red points) we show the temperature change recorded by the nanodiamond as a function of the green-laser power applied to the gold nanoparticle at a distance of 0.8 ± 0.1 μm. To verify further that the temperature change results from local heating, we repeat the measurement with the excitation laser displaced from the nanodiamond by 0.8 μm in the opposite direction. In this case, the temperature measured by the nanodiamond remained constant as a function of laser power (Fig. 3c, blue points), thereby confirming the locality of the heat source. From a linear fit to the data, we estimate the accuracy of our nitrogen–vacancy sensor to be $\delta T = 44 \pm 10$ mK. The measured temperature change agrees with the theoretically expected temperature profile based on a steady-state solution of the heat equation, $\Delta T(r) = \dot{Q}/4\pi\kappa r$, where $\dot{Q}$ is the heat dissipation, κ is the thermal conductivity of glass and r is the distance between the nanodiamond and the gold nanoparticle. As shown in Fig. 3b, by recording the temperature of six nanodiamonds at different distances from the laser-heated gold nanoparticle we find that the measured temperature profile (Fig. 3d, points) is in excellent agreement with the theoretical steady-state prediction (solid line). This allows us directly to estimate the temperature change at the location of the gold nanoparticle to be 72 ± 6 K.

To demonstrate that nanodiamond thermometry is compatible with living cells, we introduce nanodiamonds and gold nanoparticles into human embryonic fibroblast WS1 cells using nanowire-assisted delivery[15]. Just as in the control experiments described above, we probe the temperature at two different nitrogen–vacancy locations (NV_1 and NV_2) within a single cell while locally heating an individual gold nanoparticle (Fig. 4a). As shown in Fig. 4b, NV_1, which is significantly closer to the heat source, has a stronger temperature dependence as a function of laser power than does NV_2. Varying the incident power allows us to generate controlled temperature differences of up to 5 K over distances of approximately 7 μm. To ensure that this temperature gradient is created by the controlled illumination of the nanoparticle and does not result from heating of the cellular cytoplasm, we displace the laser spot from the gold nanoparticle. This results in a negligible temperature change at the location of NV_1 with $\Delta T = -20 \pm 50$ mK (Fig. 4b, green square). The increased measurement uncertainty for larger laser powers is the result of heating fluctuations from drift of the gold nanoparticle.

The experiments shown in Fig. 4b demonstrate the submicrometre measurement of an intracellular heat gradient. However, the substantial heating induced by constant illumination for an extended period of time ultimately leads to the death of the cell, which is confirmed using a standard live/dead assay (calcein AM/ethidium homodimer-1). To demonstrate that our technique can be used within living cells, we increase the concentration of gold nanoparticles to allow for heat generation at different locations simply by moving the laser focus. Then we measure the temperature variation at a single nanodiamond (Fig. 4c, bar graph) while slightly heating the gold nanoparticles in two different locations (crosses). After our measurement, the viability of the cell is confirmed (Fig. 4c).

Finally, we demonstrate that our method can be used to control cell viability. To start, we heat the cell with 12 μW of laser power and measure a temperature change of 0.5 ± 0.2 K at the nanodiamond location; this corresponds to a change of approximately 10 K at the position of the gold nanoparticle. At this point, the cell is still alive, as confirmed by the absence of ethidium homodimer-1 fluorescence inside the membrane (Fig. 4d). By increasing the laser power to 120 μW, we induce a temperature change of 3.9 ± 0.1 K at the nanodiamond location (approximately 80 K at the location of the laser focus); in this case, the cell is flooded with fluorescence from the ethidium homodimer, signalling cell death. This proof-of-principle experiment indicates that

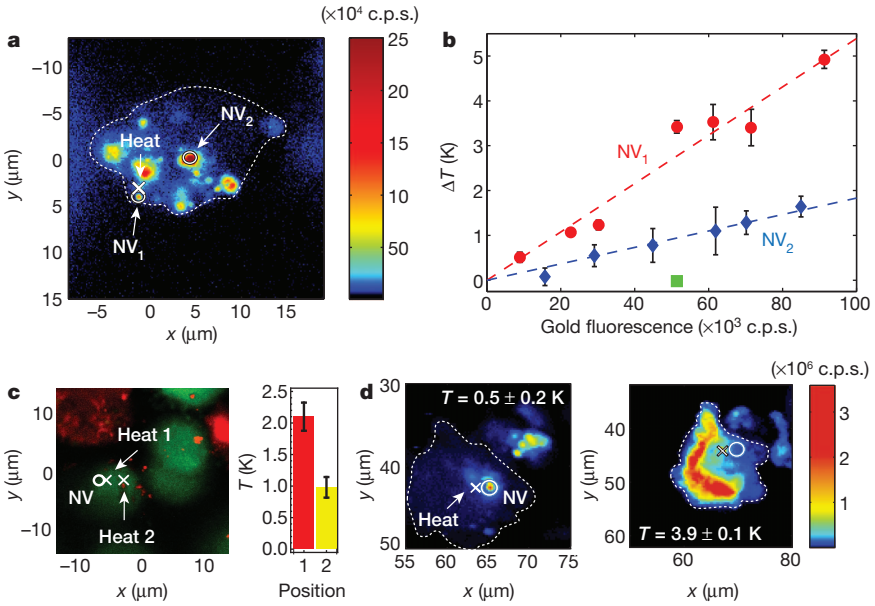

Figure 4 | Nanoscale thermometry in cells. **a**, Confocal scan of a single cell under laser excitation at a wavelength of 532 nm, with collection at wavelengths greater than 638 nm. The cross marks the position of the gold nanoparticle used for heating, and circles represent the location of the nanodiamonds (NV_1 and NV_2) used for thermometry. The dotted line provides a guide to the eye and outlines the cell membrane. Colour bars indicate the fluorescence in counts per seconds. **b**, Measured change in temperature at the positions of NV_1 and NV_2 relative to the incident laser power applied to the gold nanoparticle. Dashed lines are linear fits to the data. Each point consists of an average of five measurements, with each individual measurement taking 4 s. The error bars (1σ) are set by fluctuations in the laser heating of the gold nanoparticle. **c**, Fluorescence scan of stained cells (live/dead assay) with excitation at 494 or 528 nm and emission at 515 nm (green; live cells) and 617 nm (red; dead cells). The bar graph shows the temperature of a single nanodiamond (circle) with local heat applied at two different locations (crosses). **d**, Confocal fluorescence scans of an individual cell under varying illumination power. Excitation occurs at 532 nm and collection is above 630 nm. Cell death is indicated by the penetration of ethidium homodimer-1 through the cell membrane, staining the nucleus. At low laser powers, the cell remains alive; cell death occurs as laser-induced heating is increased.

nanodiamond thermometry may enable the optimization of nanoparticle-based photothermal therapies[8].

Our experiments demonstrate that nitrogen–vacancy centres in diamond can be used as robust temperature sensors that combine the virtues of submicrometre spatial resolution, subdegree thermal sensitivity and biocompatibility. The sensitivity of our current measurement can be enhanced by increasing the relevant coherence time or the number of nitrogen–vacancy centres within the nanocrystal, or both. Optimizing these factors should allow us to reach sensitivities of 80 $\mu K\,Hz^{-1/2}$ (Methods), yielding the ability to sense subkelvin temperature variations with millisecond time resolution. In solution, the ultimate accuracy of our method will probably be limited by residual heating during the measurement process. As discussed in the Methods, this limit is in the range of 0.05–5 mK, depending on experimental conditions. Although the present work focuses on monitoring temperature variations, the use of diamond samples with low strain, or, alternatively, ensembles of nanodiamonds, should allow for the realization of an absolute thermometer (Methods). The spatial resolution of our method can be further improved by using far-field subdiffraction techniques[26].

The present observations raise a number of intriguing possibilities. For instance, the simultaneous measurement and control of a subcellular thermal gradient could enable the accurate control of gene expression[27]. Further improvements in sensitivity may allow for real-time observations of non-equilibrium subcellular processes in biological and medical applications[11]. The large dynamic range of our quantum thermometer and its intrinsic robustness may also allow for the direct microscopic monitoring and control of chemical reactions[20]. Moreover, combining our technique with two-photon microscopy[28,29] may enable *in vivo* identification of local tumour activity by mapping atypical thermogenesis at the single-cell level[30]. Finally the combination of thermoablative therapy with our temperature sensor could be a potent tool for the selective identification and killing of malignant cells without damaging surrounding tissue[7,8].

METHODS SUMMARY

Nanodiamond measurement pulse sequence. As indicated in Fig. 3a, we record the fluorescence at four different frequencies centred on $\Delta = 2\pi \times 2.87$ GHz:

$$f^1 \approx f(\omega_-) + \left.\frac{\partial f}{\partial \omega}\right|_{\omega_-} \left(-\delta\omega + \delta\beta + \delta T \frac{d\Delta}{dT}\right)$$

$$f^2 \approx f(\omega_-) + \left.\frac{\partial f}{\partial \omega}\right|_{\omega_-} \left(\delta\omega + \delta\beta + \delta T \frac{d\Delta}{dT}\right)$$

$$f^3 \approx f(\omega_+) + \left.\frac{\partial f}{\partial \omega}\right|_{\omega_+} \left(-\delta\omega - \delta\beta + \delta T \frac{d\Delta}{dT}\right)$$

$$f^4 \approx f(\omega_+) + \left.\frac{\partial f}{\partial \omega}\right|_{\omega_+} \left(\delta\omega - \delta\beta + \delta T \frac{d\Delta}{dT}\right)$$

This allows us to determine the change in temperature:

$$\delta T = \frac{\delta\omega}{d\Delta/dT} \frac{(f^1 + f^2) - (f^3 + f^4)}{(f^1 - f^2) + (f^3 - f^4)} \quad (1)$$

Here $\omega_\pm \mp \delta\omega$ are the four microwave carrier frequencies and δB is an unknown static magnetic field. By using the fluorescence at these four frequencies as shown in equation (1), we are able to remove errors associated with changes in total fluorescence rate, ESR contrast, Rabi frequency and magnetic field.

Full Methods and any associated references are available in the online version of the paper.

Received 19 March; accepted 10 June 2013.

1. Yue, Y. & Wang, X. Nanoscale thermal probing. *Nano Rev.* http://dx.doi.org/10.3402/nano.v3i0.11586 (2012).
2. Lucchetta, E., Lee, J., Fu, L., Patel, N. & Ismagilov, R. Dynamics of *Drosophila* embryonic patterning network perturbed in space and time using microfluidics. *Nature* **434,** 1134–1138 (2005).
3. Kumar, S. V. & Wigge, P. A. H2A.Z-containing nucleosomes mediate the thermosensory response in *Arabidopsis*. *Cell* **140,** 136–147 (2010).
4. Lauschke, V. M., Tsiairis, C. D., François, P. & Aulehla, A. Scaling of embryonic patterning based on phase-gradient encoding. *Nature* **493,** 101–105 (2012).

5. Kamei, Y. *et al.* Infrared laser-mediated gene induction in targeted single cells *in vivo*. *Nature Methods* **6,** 79–81 (2009).
6. Vreugdenburg, T., Willis, C., Mundy, L. & Hiller, J. A systematic review of elastography, electrical impedance scanning, and digital infrared thermography for breast cancer screening and diagnosis. *Breast Cancer Res. Treat.* **137,** 665–676 (2013).
7. Schroeder, A. *et al.* Treating metastatic cancer with nanotechnology. *Nature Rev. Cancer* **12,** 39–50 (2011).
8. O'Neal, D. P., Hirsch, L. R., Halas, N. J., Payne, J. D. & West, J. L. Photo-thermal tumor ablation in mice using near infrared-absorbing nanoparticles. *Cancer Lett.* **209,** 171–176 (2004).
9. Majumdar, A. Scanning thermal microscopy. *Annu. Rev. Mater. Sci.* **29,** 505–585 (1999).
10. Kim, S. H. *et al.* Micro-Raman thermometry for measuring the temperature distribution inside the microchannel of a polymerase chain reaction chip. *J. Micromech. Microeng.* **16,** 526 (2006).
11. Yang, J., Yang, H. & Lin, L. Quantum dot nano thermometers reveal heterogeneous local thermogenesis in living cells. *ACS Nano* **5,** 5067–5071 (2011).
12. Vetrone, F. *et al.* Temperature sensing using fluorescent nanothermometers. *ACS Nano* **4,** 3254–3258 (2010).
13. Okabe, K. *et al.* Intracellular temperature mapping with a fluorescent polymeric thermometer and fluorescence lifetime imaging microscopy. *Nature Commun.* **3,** 705 (2012).
14. Donner, J., Thompson, S., Kreuzer, M., Baffou, G. & Quidant, R. Mapping intracellular temperature using green fluorescent protein. *Nano Lett.* **12,** 2107–2111 (2012).
15. Shalek, A. K. *et al.* Vertical silicon nanowires as a universal platform for delivering biomolecules into living cells. *Proc. Natl Acad. Sci. USA* **107,** 1870–1875 (2010).
16. Acosta, V. *et al.* Temperature dependence of the nitrogen-vacancy magnetic resonance in diamond. *Phys. Rev. Lett.* **104,** 070801 (2010).
17. Toyli, D. *et al.* Measurement and control of single nitrogen-vacancy center spins above 600 K. *Phys. Rev. X* **2,** 031001 (2012).
18. Chen, X.-D. *et al.* Temperature dependent energy level shifts of nitrogen-vacancy centers in diamond. *Appl. Phys. Lett.* **99,** 161903–161903 (2011).
19. Taylor, J. *et al.* High-sensitivity diamond magnetometer with nanoscale resolution. *Nature Phys.* **4,** 810–816 (2008).
20. Jin, C., Li, Z., Williams, R., Lee, K. & Park, I. Localized temperature and chemical reaction control in nanoscale space by nanowire array. *Nano Lett.* **11,** 4818–4825 (2011).
21. Maze, J. *et al.* Nanoscale magnetic sensing with an individual electronic spin in diamond. *Nature* **455,** 644–647 (2008).
22. Balasubramanian, G. *et al.* Nanoscale imaging magnetometry with diamond spins under ambient conditions. *Nature* **455,** 648–651 (2008).
23. Hodges, J. *et al.* Time keeping with electron spin states in diamond. *Phys. Rev. A* **87,** 032118 (2013).
24. Balasubramanian, G. *et al.* Ultralong spin coherence time in isotopically engineered diamond. *Nature Mater.* **8,** 383–387 (2009).
25. Dolde, F. *et al.* Electric-field sensing using single diamond spins. *Nature Phys.* **7,** 459–463 (2011).
26. Maurer, P. *et al.* Far-field optical imaging and manipulation of individual spins with nanoscale resolution. *Nature Phys.* **6,** 912–918 (2010).
27. Xu, G. *et al.* Identification of proteins sensitive to thermal stress in human neuroblastoma and glioma cell lines. *PLoS ONE* **7,** e49021 (2012).
28. Helmchen, F. & Denk, W. Deep tissue two-photon microscopy. *Nature Methods* **2,** 932–940 (2005).
29. Wee, T.-L. *et al.* Two-photon excited fluorescence of nitrogen-vacancy centers in proton-irradiated type Ib diamond. *J. Phys. Chem. A* **111,** 9379–9386 (2007).
30. Tsoli, M. *et al.* Activation of thermogenesis in brown adipose tissue and dysregulated lipid metabolism associated with cancer cachexia in mice. *Cancer Res.* **72,** 4372–4382 (2012).

Supplementary Information is available in the online version of the paper.

Acknowledgements We thank R. Walsworth, V. Denic, C. Latta, L. Jiang, A. Gorshkov, P. Cappellaro, A. Sushkov and I. Lovchinsky for discussions and help with experiments. This work was supported by the NSF, the Center for Ultracold Atoms, the Defense Advanced Research Projects Agency (QUASAR programme), the Army Research Office (MURI programme), the Packard Foundation, NIH Pioneer Awards (5DP1OD003893-03), the NHGRI (1P50HG006193-01) and the Swiss National Science Foundation (PBSKP2_143918) (P.C.M.).

Author Contributions P.C.M., H.J.N., H.P. and M.D.L. developed the idea for the study. G.K., P.C.M. and N.Y.Y. designed and conducted the experiments and analysed the data. M.K., P.K.L. and H.P. prepared the biological samples. All authors participated in discussions and writing of the manuscript.

Author Information Reprints and permissions information is available at www.nature.com/reprints. The authors declare no competing financial interests. Readers are welcome to comment on the online version of the paper. Correspondence and requests for materials should be addressed to H.P. (hongkun_park@harvard.edu) or M.D.L. (lukin@physics.harvard.edu).

METHODS

Experimental apparatus, sensitivity and accuracy. Our experimental apparatus consists of a confocal microscope with two independent excitation–collection paths, allowing measurement and heating at two independent locations simultaneously. The experiments use either a Nikon Plan Fluor ×100, oil immersion, NA = 1.3 objective (nanodiamonds) or a Nikon Plan Apo ×100, air, NA = 0.95 objective (bulk sample), resulting in $C \approx 0.03$, which can be further improved by employing a solid immersion lens or diamond nanopatterning. Microwaves are delivered using a lithographically defined coplanar waveguide on top of a glass coverslip. For experiments with nanodiamonds, we use neutral-density filters in the collection path to avoid saturation of the avalanche photodiode. The temperature accuracy, δT, for bulk diamond is estimated from the measurement shown in Fig. 2b. Using the standard deviation σ (plotted error bars), we determine the accuracy to be $\delta T = \sigma(2\tau c \mathrm{d}\Delta/\mathrm{d}T)^{-1}$, where c is the oscillation amplitude and 2τ is the free evolution time. We find that for integration times $t < 30$ s (limited by temperature stability) the temperature accuracy increases in proportion to $\sqrt{t}$, giving a sensitivity of $\eta = \delta T\sqrt{t}$. A linear dependence of the dissipated heat on laser power (Fig. 3b) is used to determine the measurement accuracy for nanodiamonds. A linear function, with slope m, is fitted to the data (Fig. 3c, red dashed line) and the measurement accuracy is given by $\delta T = \sqrt{\sum_{i=1}^{N}(T_i - m\,P_i)^2/(N-1)}$, where T_i is the measured temperature and P_i is the corresponding laser power. The error bars are evaluated as

$$\sigma(\delta T) = \delta T\sqrt{1 - \frac{2}{N-1}\frac{\Gamma^2(n/2)}{\Gamma^2((n-1)/2)}}$$

where $\Gamma(\cdot)$ is the Gamma distribution.

Ultimate sensitivity. The ultimate sensitivity of our method is limited by the nitrogen–vacancy coherence time and the number of defect centres. In our current experiment, we have demonstrated a sensitivity of 9 mK $\mathrm{Hz}^{-1/2}$ (with a free evolution time of 250 μs). Two natural extensions allow longer nitrogen–vacancy coherences: decreasing the ^{13}C concentration to suppress the nuclear spin bath, and further dynamical decoupling. These methods can, in principle, allow us to extend the evolution time to $T_1/2 \approx 3$ ms. In combination with a nanocrystal that contains ~1,000 nitrogen–vacancy centres, this could yield an ultimate sensitivity limit of 80 μK $\mathrm{Hz}^{-1/2}$. Further improvement may be possible by using spin-squeezed states. Finally, the determination of absolute temperature is limited by variations in the zero-field splitting due to spatially varying strain. For low-strain diamond samples, we find that the variation in the zero-field splitting is less than 60 kHz, allowing for subkelvin absolute-temperature determination. In addition, the use of an ensemble of nitrogen–vacancy centres in different nanodiamonds with uncorrelated strain values allows for a further increase in absolute sensitivity by a factor of $\sqrt{n}$, where n is the number of nanodiamonds.

Ultimate accuracy in solution. In cases where our method is used to probe a system that is in solution (for example cells and chemical reactions), the primary accuracy limit is set by heat dissipation during the measurement process. In particular, the microwave spectroscopy used to detect changes in the nitrogen–vacancy zero-field splitting also induces heating of the solution. In the present experiment, we use a lithographically fabricated microwave loop (diameter, 200 μm) to generate an a.c. magnetic field, $B \approx 10$ mG, for spin manipulations. Estimating the effective dipole field created by the microwave loop shows that the solution (water) absorbs 10^{-6} W of power, yielding a temperature increase of 5 mK in the steady state. By using a smaller microwave loop (20 μm) and reducing the duty cycle, it should be possible to decrease the heating of the solution to approximately 50 μK.

Injection of nanodiamonds into cells. Nanodiamonds and gold nanoparticles were introduced into human embryonic fibroblast WS1 cells by means of silicon-nanowire-mediated delivery[15]. Silicon nanowires were treated with 3-aminopropyltrimethoxysilane to give NH_2 functionality on the surface. Nanodiamonds and gold nanoparticles were subsequently attached by electrostatic binding. Afterwards, WS1 cells were plated on the silicon nanowire substrates and cultured overnight. The cells were removed by trypsin treatment and re-plated on a glass slide with lithographically defined strip lines for ESR measurements. The samples were stained with calcein AM and ethidium homodimer-1 for the live/dead assay.